Journal of Materials Chemistry A

PAPER

View Article Online
View Journal

Cite this: DOI: 10.1039/c8ta03987a

Ultrafine SiO_x/C nanospheres and their pomegranate-like assemblies for high-performance lithium storage†

Qiang Yu,[a] Peipei Ge,[b] Zhenhui Liu,[a] Ming Xu,[a] Wei Yang,[a] Liang Zhou,*[a] Dongyuan Zhao[a] and Liqiang Mai*[a]

Received 1st May 2018
Accepted 9th July 2018

DOI: 10.1039/c8ta03987a

rsc.li/materials-a

The application of silicon oxide (SiO_x)-based anode materials in lithium-ion batteries is hampered by their low conductivity and large volume expansion. To tackle both issues, ultrafine SiO_x/C composite nanospheres with a uniform diameter of ~40 nm were fabricated through a tri-component co-assembly approach. The ultrafine SiO_x/C nanospheres demonstrated a high specific capacity of 895 mA h g^{-1} after 200 cycles at 200 mA g^{-1}. At a high current density of 1 A g^{-1}, a capacity of 828 mA h g^{-1} could be achieved after 1000 cycles. The ultrafine SiO_x/C nanospheres were further assembled into pomegranate-like assemblies through spray drying. The resultant pomegranate-like structure manifested a discharge capacity of 1024 mA h g^{-1} after 200 cycles at 500 mA g^{-1}.

Introduction

Lithium-ion batteries (LIBs) with high energy density, low self-discharge, long cycle life, and environmental friendliness have brought great convenience to modern life.[1,2] The anode is a key component of LIBs. Various anode materials, including carbon,[3–6] metal oxides,[7,8] Si-based materials,[9] Sn-based materials,[10] and Ti-based materials[11,12] have been extensively studied. Among the diverse anode materials, graphite and $Li_4Ti_5O_{12}$ have received great commercial success owing to their low price and excellent cyclability. However, their relatively low capacities (graphite: 372 mA h g^{-1} and $Li_4Ti_5O_{12}$: 175 mA h g^{-1}) cannot meet the requirements of next-generation LIBs. Therefore, significant efforts have been devoted to exploiting novel low-cost and high-capacity anode materials.[6,13–15]

Recently, silicon oxides (SiO_x) have received great attention as promising anode materials for next-generation LIBs.[16–25] Their merits include high theoretical capacity (1965 mA h g^{-1} for SiO_2 and 2680 mA h g^{-1} for SiO), appropriate working potential, rich abundance, and low cost. Unfortunately, the high capacity of SiO_x is accompanied by a large volume fluctuation during lithiation/de-lithiation, leading to electrode pulverization and thus severe capacity decay.[26,27] Besides, the SiO_x have low intrinsic electrical conductivity, which limits their rate performance.

Several strategies have been proposed to address the volume variation and conductivity issues of SiO_x. An effective strategy is to reduce the particle size of SiO_x, which alleviates the strain induced by volume change and improves the cycling stability.[28,29] Another strategy is to coat the SiO_x nanoparticles with carbon, which enhances the electrical conductivity.[30–32] Although the carbon coated SiO_x nanoparticles show improved cyclability and rate capability, the nanoparticles suffer from severe aggregation, high inter-particle resistance, and low tap density. Assembling primary nanoparticles into pomegranate-like structures has been demonstrated to be effective in overcoming the drawbacks of nanoparticles without compromising their merits.[9,33] However, such pomegranate-like structures have not been reported for SiO_x-based anode materials to the best of our knowledge.

Herein, we report the synthesis of ultrafine SiO_x/C composite nanospheres with a uniform diameter of ~40 nm *via* a tri-component co-assembly approach. With an ultrafine size for ion diffusion, conductive carbon coating for volume expansion accommodation and electrical conductivity enhancement, the resultant SiO_x/C nanospheres manifested a high capacity (895 mA h g^{-1} after 200 cycles at 200 mA g^{-1}) and outstanding cycling stability (828 mA h g^{-1} after 1000 cycles at 1 A g^{-1}). The nanospheres were further assembled into pomegranate-like microspheres through spray drying. The

[a]State Key Laboratory of Advanced Technology for Materials Synthesis and Processing, Wuhan University of Technology, Wuhan 430070, P. R. China. E-mail: liangzhou@whut.edu.cn; mlq518@whut.edu.cn

[b]College of Materials Science and Engineering, Qingdao University of Science and Technology, Qingdao 266042, P. R. China

† Electronic supplementary information (ESI) available: Digital photo of the SiO_2 colloidal solution; SEM images of SiO_2/resin and SiO_x/C; HRTEM image of the SiO_x/C-2; XPS spectrum of SiO_x/C-2; FT-IR spectrum of SiO_2/resin; cyclic voltammetry and EIS curves of SiO_x/C; cycling performance of hollow carbon spheres; SEM and TEM images of the pomegranate-like SiO_2/resin; N_2 sorption results and EDS elemental mappings of the pomegranate-like SiO_x/C-2. See DOI: 10.1039/c8ta03987a

obtained pomegranate-like SiO_x/C microspheres presented a high capacity of 1024 mA h g^{-1} after 200 cycles at 500 mA g^{-1}.

Experimental

Synthesis of SiO_x/C composite nanospheres

Firstly, 0.2 g 3-aminophenol, 0.255 g hexamethylenetetramine (HMTA), and 0.15 g cetyltrimethyl ammonium bromide (CTAB) were dissolved in 20 mL deionized water. Then, 1.2 mL tetrapropyl orthosilicate (TPOS) was added dropwise and stirred for 10 min. The mixed solution was heated to 85 °C and kept for 24 h under constant stirring. The SiO_2/resin nanospheres were collected by centrifugation, washed with deionized water and ethanol, and dried. To obtain SiO_x/C nanospheres, the SiO_2/resin was annealed at 800 °C for 5 h in N_2.

To prepare pomegranate-like SiO_x/C microspheres, the as-synthesized SiO_2/resin nanospheres were dispersed in deionized water and ultrasonicated for 12 h. The suspension was then spray dried using a Buchi mini spray drier B-290. After carbonization in N_2, pomegranate-like SiO_x/C microspheres can be obtained.

Characterization

X-ray diffraction (XRD) patterns were obtained on a D8 Advance X-ray diffractometer. Field-emission scanning electron microscopy (FESEM) images were conducted on a JEOL-7100F scanning electron microscope. Transmission electron microscopy (TEM) images and energy dispersive X-ray spectroscopy (EDS) elemental mappings were collected on a JEM-2100F microscope. The BET surface areas and pore volumes were calculated from N_2 sorption results, which were measured on a Tristar-3020 instrument at 77 K. Raman spectra were recorded with a micro-Raman spectroscopy system (Renishaw INVIA). The carbon content was obtained from thermogravimetric (TG) (NETZSCH STA 449F5) measurements, during which the samples were heated to 800 °C in air with a heating rate of 10 °C min^{-1}. X-ray photoelectron spectroscopy (XPS) results were obtained using a VG MultiLab 2000 instrument.

Electrochemical measurements

A slurry containing SiO_x/C nanocomposites (70 wt%), acetylene black (20 wt%), and sodium alga acid (10 wt%) was coated evenly on copper foil. The obtained film was dried at 70 °C for 12 h. The coin cells (2016-type) were assembled in a glove-box filled with Ar. Li chips and glass fiber were used as the counter electrode and membrane, respectively. 1 M $LiPF_6$ dissolved in ethylene carbonate (EC), dimethyl carbonate (DMC), and diethyl carbonate (DEC) (1 : 1 : 1 in volume) was used as the electrolyte. The mass loading of the active material was 1–1.5 mg cm^{-2}. The cells were aged for 12 h before testing. Cyclic voltammetry (CV) curves were obtained on a CHI 600E electrochemical workstation between 0.01 and 3.0 V at a scan rate of 0.1 mV s^{-1}. Galvanostatic charge–discharge (GCD) measurements were performed on a NEWARE testing system. Electrochemical impedance spectroscopy (EIS) data were collected on an Autolab PGSTAT 302N in a frequency range of 0.01–100 kHz.

Results and discussion

The synthesis of ultrafine SiO_x/C nanospheres was realized through a tri-component co-assembly approach using TPOS, 3-aminophenol, CTAB, and HMTA as the precursors (Fig. 1). First, 3-aminophenol catalyzed the hydrolysis and condensation of TPOS at room temperature, generating ultrafine SiO_2 colloids (Fig. S1†). With positively charged head groups, the CTAB molecules tend to be absorbed on the negatively charged surface of the SiO_2 colloids. When the temperature was gradually increased, the HMTA began to hydrolyze, generating ammonia and formaldehyde. The 3-aminophenol then polymerized with the *in situ* generated formaldehyde, forming a 3-aminophenol–formaldehyde resin coating layer on the SiO_2 surface (SiO_2/resin). After carbonization at 800 °C in N_2, SiO_x/C nanospheres were obtained. To obtain pomegranate-like SiO_x/C microspheres, the as-synthesized SiO_2/resin nanospheres were first spray dried and then carbonized.

The as-synthesized SiO_2/resin-2 (synthesized with a TPOS dosage of 1.2 mL) is comprised of uniform nanospheres with an average size of ~46 nm (Fig. 2a, b, S2†). After carbonization, the SiO_2/resin-2 is converted into SiO_x/C-2 with a well-preserved spherical morphology; meanwhile, the particle size reduces from 46 to 40 nm owing to the thermal induced shrinkage of resin (Fig. 2c, d). Because of the high surface energy of the nanospheres, both SiO_2/resin-2 and SiO_x/C-2 show a certain degree of aggregation. EDS elemental mapping is employed to reveal the elemental distribution of SiO_x/C-2 (Fig. 2g–l). The C and N distribute homogeneously, while the Si and O mainly disperse in the core region of the composite nanospheres, suggesting the core@shell structure of SiO_x/C-2. The HRTEM images of SiO_x/C-2 are provided in Fig. S3.† However, it is very difficult to observe the interface between SiO_x and carbon in the HRTEM images because both SiO_x and carbon are generally amorphous. The formation of such a SiO_x/C core@shell structure is caused by the sequential condensation of SiO_2 and polymerization of 3-aminophenol/formaldehyde. To further confirm the core@shell structure, the SiO_x/C-2 is treated with an excess amount of HF. The HF treatment removes the SiO_x and leaves behind a hollow carbon shell, unambiguously demonstrating the core@shell structure of SiO_x/C-2 (Fig. 2e, f). From the cavity size of the hollow carbon shells, it can be deduced that the size of SiO_x in SiO_x/C-2 is less than 20 nm.

To reveal the effects of the amount of TPOS, its dosage is tuned from 0.9 to 1.5 mL with other synthetic conditions unchanged (Table S1†). In general, the introduction of more TPOS induces the formation of more nuclei and thus a smaller particle size. With a low TPOS dosage of 0.9 mL, the obtained SiO_x/C-1 nanospheres show an average particle size of 42 nm (Fig. S4†). With a high TPOS dosage of 1.5 mL, the resultant SiO_x/C-3 nanospheres show an average size of 36 nm (Fig. S5†). Besides ultrafine SiO_x/C nanospheres, micron-sized SiO_2 particles can also be observed in SiO_x/C-3 (Fig. S5†), suggesting the occurrence of phase separation during sol–gel synthesis. According to previous literature,[22] such bulk SiO_2 particles have little electrochemical activity for lithium storage.

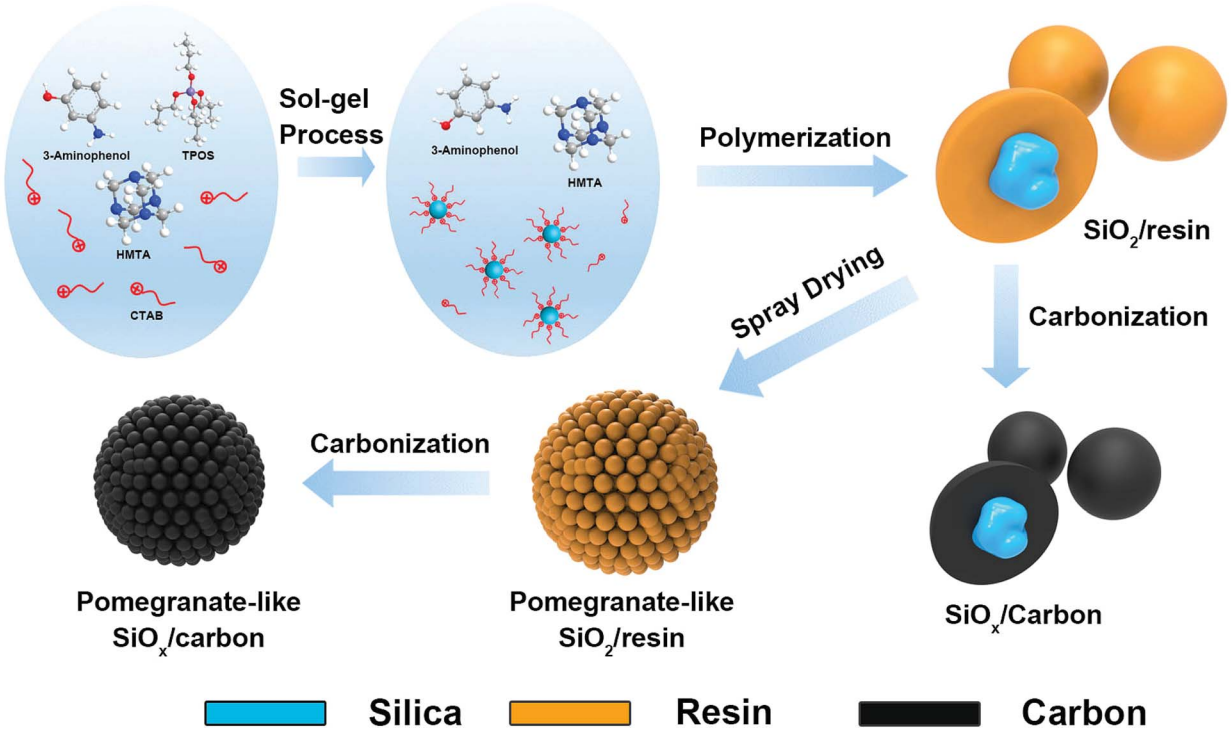

Fig. 1 Schematic illustration showing the sol–gel synthesis of ultrafine SiO_x/C composite nanospheres and spray-drying assisted synthesis of SiO_x/C pomegranate-like microspheres.

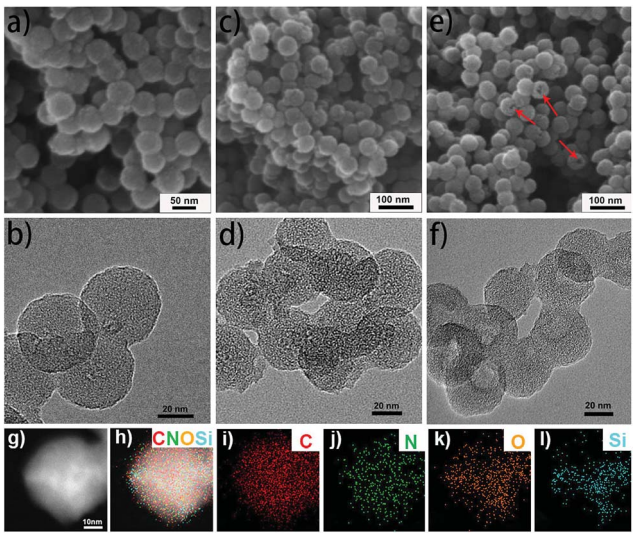

Fig. 2 SEM and TEM images of SiO_2/resin-2 (a and b), SiO_x/C-2 (c and d), and hollow carbon spheres obtained by etching SiO_x/C-2 with HF (e and f); EDS elemental mappings of C, N, O, and Si in a single SiO_x/C-2 nanosphere (g–l).

More structural information can be obtained from XRD and Raman spectroscopy. All three SiO_x/C samples show similar XRD patterns with broad diffraction peaks centered at 24 and 43° (Fig. 3a), which are characteristic of amorphous carbon. The Raman spectra (Fig. 3b) of the samples display relatively broad peaks located at ~1340 cm^{-1} and ~1590 cm^{-1}, which are associated with the D-band and G-band of the carbonaceous materials, respectively. The graphitization degree of carbon materials can be generally acquired from the I_D/I_G ratio. The three samples exhibit comparable and relatively high I_D/I_G ratios, (1.01–1.07), indicating the amorphous feature of carbon. TG analysis was employed to determine the C content of the products. The SiO_x/C-1, 2, and 3 show a relatively high C content of 78.65, 73.77, and 71.49% (Fig. 3c), respectively. The high C content is beneficial for electronic conductivity improvement and volume change buffering during the electrochemical lithiation/de-lithiation processes. The BET surface areas and

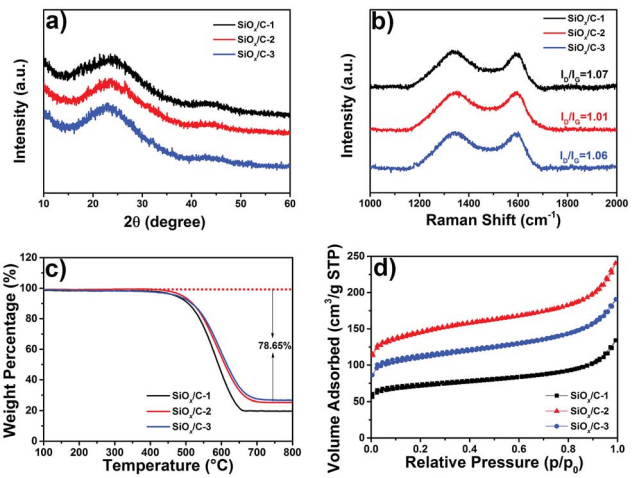

Fig. 3 XRD patterns (a), Raman spectra (b), TGA curves (c), and N_2 adsorption/desorption isotherms (d) of SiO_x/C nanocomposites.

porosity are studied by N_2 sorption analysis (Fig. 3d). The SiO_x/C samples manifest typical type I N_2 adsorption–desorption isotherms, implying their microporous feature. Such a microporous structure is advantageous for the electrolyte to access the active SiO_x sites. The BET surface areas of SiO_x/C-1, 2, and 3 are determined to be 232.8, 475.7, and 361.3 $m^2 g^{-1}$ (Table S2†), respectively. Due to the existence of bulk SiO_2 particles, the SiO_x/C-3 with the smallest nanosphere size does not possess the highest specific surface area.

The surface elemental composition of SiO_x/C-2 is determined by XPS. The survey spectrum (Fig. 4a) reveals the presence of C (75.85%), N (6.1%), O (13.67%), and Si (4.39%). The high-resolution C 1s spectrum (Fig. 4b) contains three components: sp2-bonded C (284.6 eV), C–O and C–N bonds (285.9 eV), and C=O bonds (288.4 eV).[34] The N 1s spectrum (Fig. 4c) can be deconvoluted into four peaks: pyridinic N (398.2 eV), pyrrolic N (400.6 eV), quaternary N (401.4 eV), and pyridine N–O moieties (405.2 eV).[35] The Si 2p spectrum (Fig. 4d) shows two types of Si species: the Si^{4+} located at 104.4 eV (65.1%) and Si^{3+} centered at 103.5 eV (34.9%).[19] From the high-resolution Si 2p spectrum, the average valance state of Si is calculated to be 3.65, and the x value in SiO_x/C-2 is determined to be 1.83. However, general XPS analysis only shows the elemental composition of the surface. To verify the reduction of SiO_2 to SiO_x, the sample (SiO_x/C-2) is subjected to Ar^+ etching before XPS measurements with the result shown in Fig. S6.† From Fig. S6,† the average valence state of Si is calculated to be 2.82, demonstrating the successful reduction of SiO_2 to SiO_x in the core. It should be pointed out that it is very difficult to reduce bulk SiO_2 to SiO_x through carbothermal reduction at 800 °C. In our case, the ultrafine size of SiO_2 and intimate encapsulation with resin enables the successful reduction of SiO_2 to SiO_x at a relatively low temperature of 800 °C.

The lithium storage performances of the SiO_x/C nanospheres are evaluated in half cells. Fig. S8† presents the CV curves of SiO_x/C-2. Three reduction peaks can be clearly discerned in the first cathodic process. The peak at 1.05 V is ascribed to the irreversible reactions between Li and SiO_x, which generate lithium silicates, Si, and Li_2O. The peak located at 0.71 V can be assigned to the electrolyte decomposition and formation of a solid electrolyte interface (SEI). The sharp peak below 0.25 V is relevant to the alloying reaction between Si and Li ($Si + 4.4Li^+ + 4e^- \leftrightarrow Li_{4.4}Si$). The first two peaks only appear in the first cathodic process, suggesting that the corresponding reactions are irreversible. The third cathodic peak appears in the subsequent cycles, indicating the good reversibility of the alloying reaction between Si and Li.

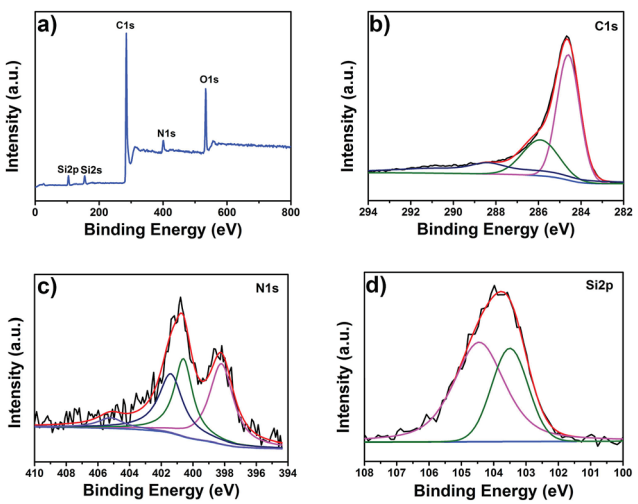

Fig. 4 XPS survey spectrum (a); high-resolution C 1s (b), N 1s (c) and Si 2p (d) spectra of SiO_x/C-2.

Fig. 5a and b display the representative discharge/charge curves and cycling stability of SiO_x/C-2 at 200 mA g^{-1}. The first discharge and charge capacities of SiO_x/C-2 reach 1829 and 1107 mA h g^{-1}, respectively. And the initial coulombic efficiency (ICE) is 61%. The relatively low ICE results from the formation of the SEI as well as the irreversible reactions between SiO_2 and Li during the first cycle. Although the ICE of SiO_x/C-2 is relatively low for practical applications, it might be further improved through controlled pre-lithiation.[36] The CE increases to 98% in the second cycle and remains at ~100% in the following cycles (Fig. 5b). As for the cycling stability, the capacity of SiO_x/C-2 decreases slightly in the initial 10 cycles and then stabilizes at ~900 mA h g^{-1}. Even after 200 cycles at 200 mA g^{-1}, a high specific capacity of 895 mA h g^{-1} can be achieved (Fig. 5b).

Fig. 5c shows the cycling performances of the SiO_x/C nanospheres at 500 mA g^{-1}. All the samples manifest stable cycling performance, and the SiO_x/C-2 shows the highest specific capacity. It delivers a capacity of 872 mA h g^{-1} after 200 cycles at 500 mA g^{-1}, higher than those of SiO_x/C-1 (481 mA h g^{-1}) and SiO_x/C-3 (683 mA h g^{-1}). The ultrafine particle size (40 nm) and SiO_x domain size (<20 nm) are responsible for the highest electrochemical activity of SiO_x/C-2. For comparison, the cycling performance of hollow carbon nanospheres prepared by etching SiO_x/C-2 nanospheres with HF is also measured (Fig. S9†). The hollow carbon spheres deliver a specific capacity of 550 mA h g^{-1} after 200 cycles at 500 mA g^{-1}. Although the SiO_x/C-3 shows a smaller particle size, the bulk SiO_2 in the samples sacrifices the capacity. The long-term cycling stability of SiO_x/C-2 at 1 A g^{-1} is also determined (Fig. 5d). Interestingly, the capacity increases slightly with cycling and reaches 828 mA h g^{-1} after 1000 cycles. According to previous studies,[37,38] the capacity increase during cycling is associated with the reversible growth/dissolution of a polymeric gel-like film.

The rate performance of SiO_x/C-2 is evaluated by varying the current density from 100 to 2000 mA g^{-1} (Fig. 5e). The specific capacities reach 1160, 880, 706, 612, and 532 mA h g^{-1} at current densities of 100, 200, 500, 1000, and 2000 mA g^{-1}, respectively. In addition, when the current density returns back to 100 mA g^{-1}, a capacity of ~1000 mA h g^{-1} can be recovered.

To obtain more information on the electrode dynamics of the SiO_x/C composite, EIS is performed. The Nyquist plots (Fig. S10†) exhibit a depressed semicircle and a quasi-straight line in high- and low-frequency regions, respectively. The diameter of the semicircle represents the charge transfer resistance (R_{ct}).[39] The SiO_x/C-2 shows an obviously smaller semicircle than those of SiO_x/C-1 and 3, suggesting its smaller charge transfer resistance.

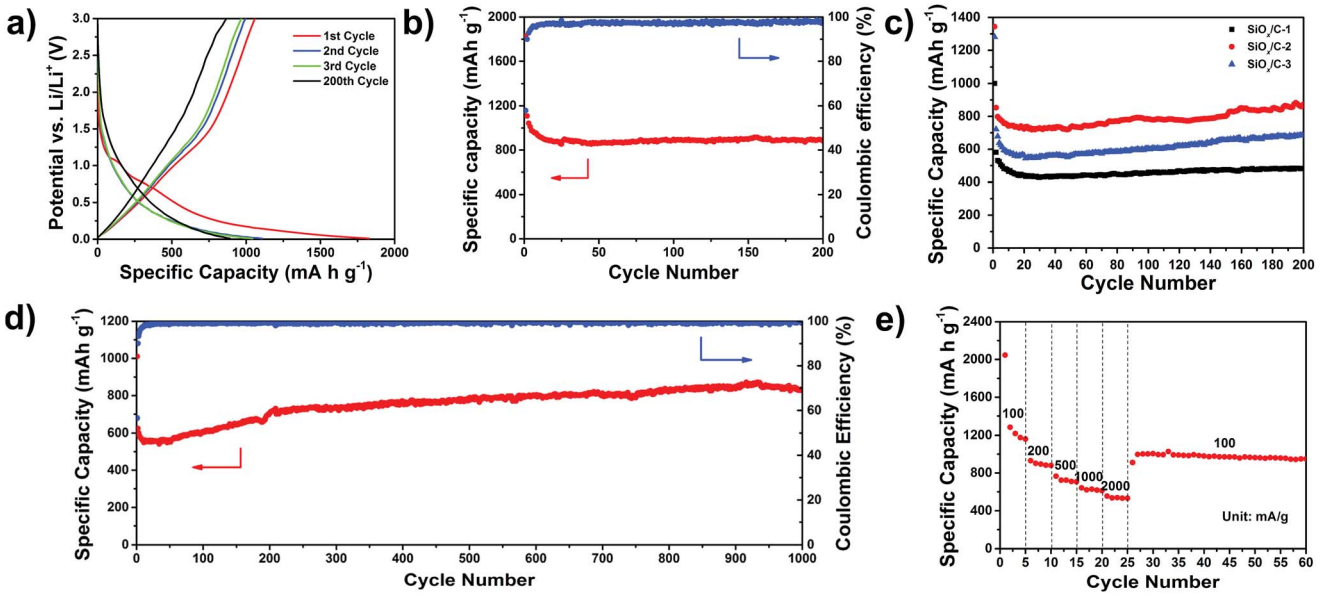

Fig. 5 Representative discharge/charge curves (a) and cycling performance (b) of SiO_x/C-2 nanospheres at a current density of 200 mA g^{-1}, cycling performances of the three SiO_x/C samples at a current density of 500 mA g^{-1} (c), long-term cycling performance of SiO_x/C at 1000 mA g^{-1} (d), and the rate performance of SiO_x/C-2 (e).

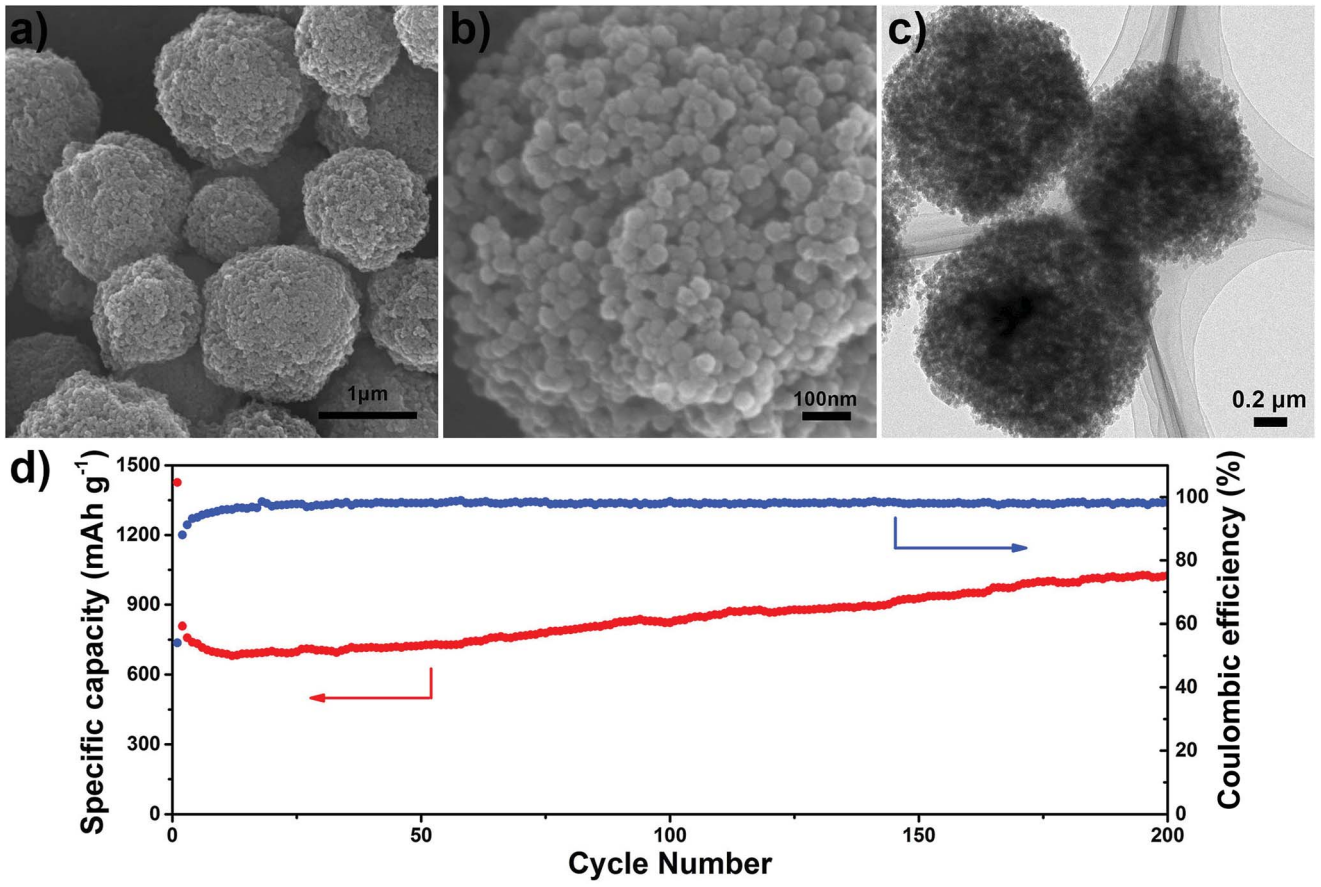

Fig. 6 SEM images (a and b), TEM image (c), and cycling performance of the pomegranate-like SiO_x/C microspheres at a current density of 500 mA g^{-1} (d).

Despite the multiple merits of nanospheres (high electrochemical activity and reduced charge transfer paths), they suffer from aggregation, high inter-particle resistance, and low tap density. To integrate the advantages of both nanospheres and micron-sized materials, we adopt a spray drying method to assemble the SiO_2/resin-2 nanospheres into microspheres (Fig. S11†) and obtain pomegranate-like SiO_x/C-2 eventually. The pomegranate-like SiO_x/C-2 microspheres have sizes of 1–5 μm and a rough nanoparticulate surface (Fig. 6a–c). Each microsphere is built up with numerous ultrafine nanospheres. The ultrafine size of SiO_x/C-2 building blocks provides the pomegranate-like SiO_x/C-2 a large BET surface area of 404 $m^2\ g^{-1}$ (Fig. S12 and Table S2†). The EDS elemental mappings show the coexistence of C, N, O, and Si in the pomegranate-like SiO_x/C-2 (Fig. S13†). When employed as the anode, the pomegranate-like SiO_x/C-2 demonstrates a reversible specific capacity of 808 mA h g^{-1} at 500 mA g^{-1}. Upon cycling, the capacity increases slightly, reaching 1024 mA h g^{-1} after 200 cycles.

When compared to most of the SiO_x-based anode materials in the literature, the SiO_x/C-2 demonstrates comparable (if not better) lithium storage performances in terms of capacity and cyclability (Table S3†). In the SiO_x/C-2 nanocomposites, the SiO_x core functions as the major active constituent, providing a high capacity to the nanocomposite. In addition, the carbon shell acts as the secondary active component, enhances the electrical conductivity of the nanocomposite, and buffers the volume expansion of SiO_x during lithiation/de-lithiation. The ultrafine particle size of SiO_x/C-2 reduces the Li ion diffusion lengths, while the rich inter-particle voids accelerate Li ion diffusion. As a result, the SiO_x/C-2 nanospheres manifest high specific capacity and outstanding cyclability. Assembling the SiO_x/C-2 nanospheres into pomegranate-like microspheres avoids the issues associated with nanosized particles without compromising the electrochemical performances.

Conclusions

In conclusion, ultrafine SiO_x/C nanospheres (~40 nm) have been synthesized through a tri-component self-assembly approach. The resultant SiO_x/C nanospheres exhibit a superior specific capacity (895 mA h g^{-1} after 200 cycles at 200 mA g^{-1}) and outstanding cycling stability (1000 cycles at 1 A g^{-1}). Pomegranate-like SiO_x/C microspheres have been constructed by a spray drying approach. The pomegranate-like SiO_x/C also exhibits superior lithium storage performances, delivering a capacity of 1024 mA h g^{-1} after 200 cycles at 500 mA g^{-1}. The facile synthesis and impressive electrochemical performances make the pomegranate-like SiO_x/C microspheres an attractive anode material for next-generation LIBs.

Conflicts of interest

There are no conflicts to declare.

Acknowledgements

This work was supported by the National Key Research and development program of China (2018FYB0104202, 2016YFA0202603), the National Natural Science Foundation of China (21673171, 51502226), the Programme of Introducing Talents of Discipline to Universities (B17034), and the National Natural Science Fund for Distinguished Young Scholars (51425204).

References

1 L. Mai, M. Yan and Y. Zhao, *Nature*, 2017, **546**, 469.
2 B. Dunn, H. Kamath and J. M. Tarascon, *Science*, 2011, **334**, 928.
3 J. I. Yamaki, M. Egashira and S. Okada, *J. Electrochem. Soc.*, 2000, **147**, 460–465.
4 M. Yoshio, H. Wang, K. Fukuda, Y. Hara and Y. Adachi, *J. Electrochem. Soc.*, 2000, **147**, 1245–1250.
5 H. Fujimoto, A. Mabuchi, K. Tokumitsu, N. Chinnasamy and T. Kasuh, *J. Power Sources*, 2011, **196**, 1365–1370.
6 L. Qie, W. M. Chen, Z. H. Wang, Q. G. Shao, X. Li, L. X. Yuan, X. L. Hu, W. X. Zhang and Y. H. Huang, *Adv. Mater.*, 2012, **24**, 2047–2050.
7 L. Zhang, H. B. Wu and X. W. Lou, *Adv. Energy Mater.*, 2014, **4**, 1300958.
8 Y. Yao, J. Li, Q. An, L. Mai and L. Zhou, *General Chemistry*, 2017, **3**, 172–181.
9 N. Liu, Z. Lu, J. Zhao, M. T. McDowell, H.-W. Lee, W. Zhao and Y. Cui, *Nat. Nanotechnol.*, 2014, **9**, 187–192.
10 H. Zhang, X. Huang, O. Noonan, L. Zhou and C. Yu, *Adv. Funct. Mater.*, 2017, **27**, 1606223.
11 Z. Chen, I. Belharouak, Y. K. Sun and K. Amine, *Adv. Funct. Mater.*, 2013, **23**, 959–969.
12 G. N. Zhu, Y. G. Wang and Y. Y. Xia, *Energy Environ. Sci.*, 2012, **5**, 6652–6667.
13 M. Ko, S. Chae, J. Ma, N. Kim, H.-W. Lee, Y. Cui and J. Cho, *Nat. Energy*, 2016, **1**, 16113.
14 D. Lin, Z. Lu, P.-C. Hsu, H. R. Lee, N. Liu, J. Zhao, H. Wang, C. Liu and Y. Cui, *Energy Environ. Sci.*, 2015, **8**, 2371–2376.
15 S. Zhu, J. Li, X. Deng, C. He, E. Liu, F. He, C. Shi and N. Zhao, *Adv. Funct. Mater.*, 2017, **27**, 1605017.
16 W.-S. Chang, C.-M. Park, J.-H. Kim, Y.-U. Kim, G. Jeong and H.-J. Sohn, *Energy Environ. Sci.*, 2012, **5**, 6895.
17 Q. Xu, J.-K. Sun, Y.-X. Yin and Y.-G. Guo, *Adv. Funct. Mater.*, 2018, **28**, 1705235.
18 M. Li, Y. Zeng, Y. Ren, C. Zeng, J. Gu, X. Feng and H. He, *J. Power Sources*, 2015, **288**, 53–61.
19 Y. Ren and M. Li, *J. Power Sources*, 2016, **306**, 459–466.
20 P. Lv, H. Zhao, J. Wang, X. Liu, T. Zhang and Q. Xia, *J. Power Sources*, 2013, **237**, 291–294.
21 Z. Li, Q. He, L. He, P. Hu, W. Li, H. Yan, X. Peng, C. Huang and L. Mai, *J. Mater. Chem. A*, 2017, **5**, 4183–4189.
22 Z. Liu, D. Guan, Q. Yu, L. Xu, Z. Zhuang, T. Zhu, D. Zhao, L. Zhou and L. Mai, *Energy Storage Materials*, 2018, **13**, 112–118.

23 C. Tang, Y. Liu, C. Xu, J. Zhu, X. Wei, L. Zhou, L. He, W. Yang and L. Mai, *Adv. Funct. Mater.*, 2018, **28**, 1704561.
24 L. Zhang, J. Deng, L. Liu, W. Si, S. Oswald, L. Xi, M. Kundu, G. Ma, T. Gemming and S. Baunack, *Adv. Mater.*, 2014, **26**, 4527–4532.
25 W. An, J. Fu, J. Su, L. Wang, X. Peng, K. Wu, Q. Chen, Y. Bi, B. Gao and X. Zhang, *J. Power Sources*, 2017, **345**, 227–236.
26 Y. Liang, L. Cai, L. Chen, X. Lin, R. Fu, M. Zhang and D. Wu, *Nanoscale*, 2015, **7**, 3971.
27 X. Cao, X. Chuan, R. C. Masse, D. Huang, S. Li and G. Cao, *J. Mater. Chem. A*, 2015, **3**, 22739–22749.
28 B. Gao, S. Sinha, L. Fleming and O. Zhou, *Adv. Mater.*, 2010, **13**, 816–819.
29 J. Tu, Y. Yuan, P. Zhan, H. Jiao, X. Wang, H. Zhu and S. Jiao, *J. Phys. Chem. C*, 2012, **118**, 7357–7362.
30 B. Guo, J. Shu, Z. Wang, H. Yang, L. Shi, Y. Liu and L. Chen, *Electrochem. Commun.*, 2008, **10**, 1876–1878.
31 Y. Yu, J. Zhang, L. Xue, T. Huang and A. Yu, *J. Power Sources*, 2011, **196**, 10240–10243.
32 J. Wang, H. Zhao, J. He, C. Wang and J. Wang, *J. Power Sources*, 2011, **196**, 4811–4815.
33 W. Li, Z. Liang, Z. Lu, H. Yao, Z. W. Seh, K. Yan, G. Zheng and Y. Cui, *Adv. Energy Mater.*, 2015, **5**, 1500211.
34 J. Wang, H. Liu, J. Diao, X. Gu, H. Wang, J. Rong, B. Zong and D. S. Su, *J. Mater. Chem. A*, 2015, **3**, 2305–2313.
35 N. P. Wickramaratne, J. Xu, M. Wang, L. Zhu, L. Dai and M. Jaroniec, *Chem. Mater.*, 2014, **26**, 2820–2828.
36 H. Kim, S. Choi, S. Lee, M. Seo, J. G. Lee, E. Deniz, Y. Lee, E. Kim and J. Choi, *Nano Lett.*, 2016, **16**, 282.
37 S. Laruelle, S. Grugeon, P. Poizot, M. Dollé, L. Dupont and J. M. Tarascon, *J. Electrochem. Soc.*, 2002, **149**, A627–A634.
38 S. Grugeon, S. Laruelle, L. Dupont and J. M. Tarascon, *Solid State Sci.*, 2003, **5**, 895–904.
39 X. Cao, X. Chuan, S. Li, D. Huang and G. Cao, *Part. Part. Syst. Charact.*, 2016, **33**, 110–117.